Efficient Thermal Noise Removal for Sentinel-1 TOPSAR Cross-Polarization Channel

Jeong-Won Park, *Member, IEEE*, Anton A. Korosov, Mohamed Babiker, Stein Sandven, and Joong-Sun Won, *Senior Member, IEEE*

***Abstract*— The intensity of a Sentinel-1 Terrain Observation with Progressive Scans synthetic aperture radar image is disturbed by additive thermal noise, particularly in the cross-polarization channel. Although the European Space Agency provides calibrated noise vectors for noise power subtraction, residual noise contributions are significant when considering the relatively narrow backscattering distribution of the cross-polarization channel. In this paper, we investigate the characteristics of noise and propose an efficient method for noise reduction based on a three-step correction process comprised of azimuth descalloping, noise scaling and interswath power balancing, and local residual noise power compensation. The core idea is to find the optimal correction coefficients resulting in the most noise-uncorrelated gentle backscatter profile over a homogeneous region and to combine them with the scalloping gain for a reconstruction of the complete 2-D noise field. Denoising is accomplished by subtracting the reconstructed noise field from the original image. The performance improvement in some applications by adopting the denoising procedure shows the effectiveness of the proposed method.**

***Index Terms*— Cross polarization, denoising, scalloping, Sentinel-1, Terrain Observation with Progressive Scans synthetic aperture radar (TOPSAR), thermal noise.**

I. Introduction

RADIOMETRIC correction is one of the most important preprocessing steps that must be done precisely to assure the quality of the results retrieved from satellite imagery. Recent spaceborne synthetic aperture radar (SAR) systems, such as Sentinel-1A/B, RADARSAT-2, and TerraSAR-X/TanDEX-X, are not only well calibrated, but they also provide vectors of the noise equivalent sigma nought (NESZ) for the further correction of additive noise [1]–[3]. Thermal noise is the additive background energy that causes a noise floor [4]. Since any signal below this level is indistinguishable from noise, the calibrated thermal noise power can be interpreted similar to the NESZ. Thermal noise throughout an image varies along both the range and azimuth axes, since the noise power in raw data is modified by range-varying correction factors and antenna power normalization [5]. In multiswath observation modes such as Scanning SAR (ScanSAR) and Terrain Observation with Progressive Scans SAR (TOPSAR), different noise patterns in each subswath cause additional problems, namely, discontinuous sharp changes in the intensity at interswath boundaries. The operational observation mode of Sentinel-1 SAR is TOPSAR, which can achieve the same coverage and resolution as ScanSAR but with a nearly uniform signal-to-noise ratio (SNR) and distributed target ambiguity ratio [6], [7] by taking an advantage of the full azimuth aperture by sweeping the antenna beam forward in each burst (see Fig. 1). The scalloping power of ScanSAR varies by a few decibels, while that of TOPSAR is much less under standard SAR processing [8]. With postprocessing techniques, including descalloping, the signal power is normalized well, but the additive thermal noise power is further shaped by the application of postprocessing gains. Thus, thermal noise in TOPSAR varies two-dimensionally and includes three main features: elevation angle-dependent range variation, interswath discontinuities, and burstwise variation (scalloping).

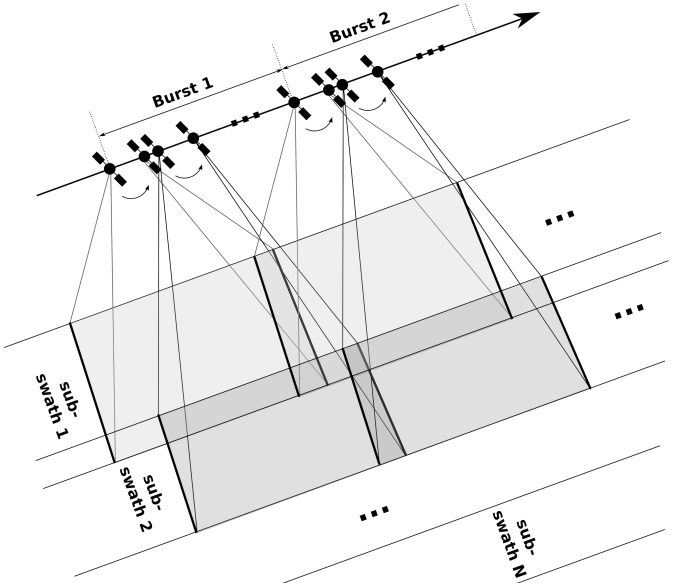

Fig. 1. Scanning geometry of the TOPSAR system. In the case of the extended wide swath mode of Sentinel-1, the number of subswaths is 5. In each burst, the antenna beam sweeps forward along the azimuth direction for each subswath. Overlapping happens in between both bursts and subswaths.

Dual-polarization (HH/HV or VV/VH) observations have recently become common in spaceborne SAR systems, since the use of cross-polarization channels generates a potential

Manuscript received September 27, 2016; revised April 4, 2017 and July 3, 2017; accepted October 13, 2017. Date of publication December 4, 2017; date of current version February 27, 2018. This work was supported by the Research Council of Norway and the Russian Foundation for Basic Research under NORRUSS Project 243608, SONARC.

J.-W. Park, A. Korosov, M. Babiker, and S. Sandven are with the Nansen Environmental and Remote Sensing Center, 5006 Bergen, Norway (e-mail: jeong-won.park@nersc.no).

J.-S. Won is with the Department of Earth System Sciences, Yonsei University, 03722 Seoul, South Korea.

Color versions of one or more of the figures in this paper are available online at http://ieeexplore.ieee.org.

Digital Object Identifier 10.1109/TGRS.2017.2765248

improvement for many SAR intensity-based applications, such as image classification [9], [10], target detection [11], [12], and geophysical parameter retrieval [13]–[15]. Thermal noise is hardly noticeable in copolarization channels, as the signal power is high enough for screening the variations of thermal noise in most cases. Cross-polarization channels, however, are often significantly disturbed by thermal noise, because their depolarized power is naturally weaker than their initially polarized power. Thus, precise thermal noise corrections are essential for acquiring useful information from cross-polarization channels. Since the release of Sentinel-1 Instrument Processing Facility (IPF) version 2.5, the noise vectors included in the Sentinel-1 Standard Archive Format for Europe (SAFE) format have been calibrated to support the denoising of the ground range detected (GRD) product [16]. Although the denoising process suggested by the European Space Agency (ESA) introduced a large improvement in image quality, there are remaining problems caused by an imperfection of the given noise vectors.

Previous studies concerning the correction of additive thermal noise in SAR imagery are limited. A classic approach is to subtract the empirically determined noise floor [17], [18]. This method assumes a constant noise floor from scene to scene; however, this is not true, because the mean noise power varies even in a single scene along the azimuth axis. Another approach is to compensate for local backscattering differences in a sliding window, as was proposed in [19]. Although this method showed a visual enhancement, it failed to improve the performance of the motion tracking algorithm for which the denoising method was developed. The most preferable approach is to use the given noise information if available. Since both payload control and signal processing have become precise in modern SAR systems, the spatial characteristics of the expected image noise are estimated, and it is being provided in conjunction with the delivered image products. For the fine-tuning of given noise information, a noise scaling approach [20] was proposed based on a local SNR estimation. Although this method showed a high performance for TerraSAR-X imagery, it can only handle overestimated noise and requires an adaptation for sliding patches over each image to update the optimal scaling factors. For operational use in near-real time applications or systematic calibrations, it is preferable to adopt a quick and efficient correction method without complex parameter adaptations for each specific image.

In this paper, we propose an efficient noise reduction method for the Sentinel-1 GRD product by modifying the ESA-provided noise vectors. We developed a new noise scaling method based on empirical optimization. The core idea is to find the optimal scaling factors and offsets that yield the most flattened backscatter profile along the range axis over homogeneous areas. We adopted different noise scaling factors and offsets for each subswath and integrated them with a scalloping effect to reconstruct the noise field for the complete image normalization. We used the extra wide (EW) swath product for developing and evaluating the proposed denoising method, but the same approach can be applied similar to the interferometric wide swath product as well.

In Section II, a general overview of noise-induced problems in the Sentinel-1 TOPSAR GRD product is addressed with their origins. Then, the noise subtraction results using the original ESA-provided noise vectors are briefly described, and the residual noise problems are analyzed. In Section III, methods for compensating for residual noise and interchannel power differences are introduced. Tips for reconstructing the complete 2-D noise field, including the scalloping features, are explained as well. Then, the experimental results for the optimal scaling factors and offsets determined from a statistical approach are introduced, and the benefits of the proposed noise correction method are demonstrated in Section IV. In Section V, our findings are summarized.

II. General Noise Features of Sentinel-1 TOPSAR Intensity Image

In general, an SAR image product contains not only the wanted signal but also the unwanted noise that is superposed within the same pixel. Among the various noise components in SAR systems, the thermal noise is an additive noise, which is processed with the same processing gains applied to the true signal. With P_S and P_N denoting the power of the signal and the noise, respectively, the resulting power in the GRD product is

$$P_{\mathrm{SN}} = G(P_S + P_N) \tag{1}$$

where G is the total gain applied during the formation of the SAR image. In a sense, noise compensation can be performed by simply subtracting the scaled noise power, $G \cdot P_N$, from the given combined signal and noise power, P_{SN}. Sentinel-1 TOPSAR images suffer from two types of additive noise in terms of the backscattering intensity. One is a thermal noise that changes with the antenna pattern and has a different intensity in each subswath. In multiswath acquisition modes such as ScanSAR and TOPSAR, this noise can cause an intensity step at interswath boundaries. The other is a scalloping noise with a variable burstwise intensity that changes along the azimuth direction. In the TOPSAR mode, the steering of the antenna beam in the azimuth direction causes the weighting of the echoes to vary along the azimuth direction, inducing a scalloping effect. In this section, we describe the general characteristics of these two noises.

A. Thermal Noise Variation in the Range Direction

SAR images suffer from not only speckle noise but also thermal noise, especially when the backscattered power is low. For the copolarized channel, this will not be a problem in most cases; however, for the cross-polarized channel, this is the main obstacle for analyzing an image with a low backscatter. In principle, thermal noise contamination can be eliminated simply by subtracting the noise from an intensity image. The ESA provides thermal noise information for each image product as annotated noise vectors, which are included in a Sentinel-1 SAFE format as an independent XML formatted file. Fig. 2 shows the images from before and after the application of noise correction based on the ESA-provided noise vectors. Although the noise subtraction using the

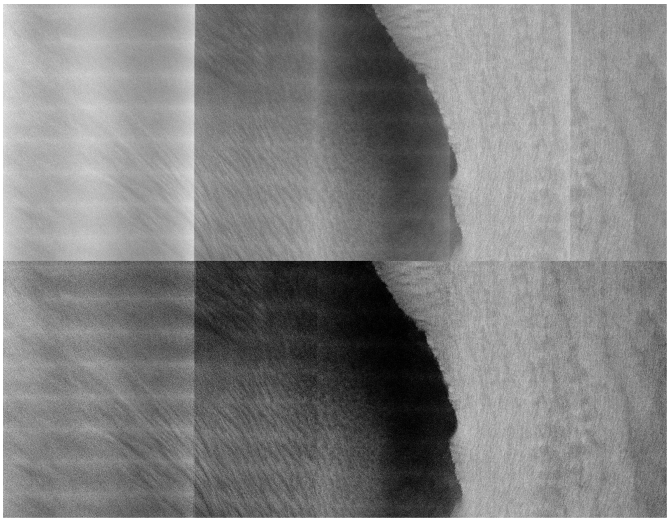

Fig. 2. Uncorrected Sentinel-1 EW HV-polarization image (Scene ID: S1A_EW_GRDM_1SDH_20151218T065121_20151218T065151_009093_00D103_EB28) over (Top) wind-roughened sea surface and (Bottom) corresponding noise correction results using the ESA-provided noise vectors.

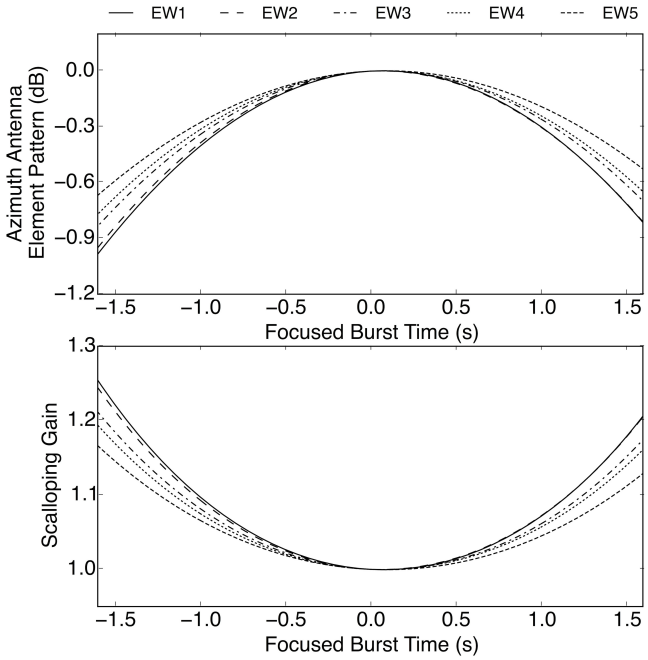

Fig. 3. Azimuth antenna element pattern of (Top) Sentinel-1A EW mode and (Bottom) corresponding scalloping effects on thermal noise.

ESA-provided noise vectors results in less-noticeable intensity steps between interswath boundaries as shown in Fig. 2, there is still a large difference between the leftmost subswath (EW1) and the next subswath (EW2). Furthermore, the intensity near the subswath boundary appears to be higher than that in the subswath center for all the subswaths.

B. Thermal Noise Scalloping in the Azimuth Direction

In the TOPSAR mode, azimuth beam steering causes an antenna gain change in the azimuth direction, which induces SAR signal scalloping that is characterized by a gain loss toward the edges of each burst. This signal gain loss is compensated by descalloping during SAR processing. As a side effect, the otherwise uniform thermal noise is amplified toward the burst edges along the azimuth direction. Although this effect is much less pronounced in TOPSAR compared with ScanSAR, it still can be seen when the backscattering intensity is weak. In Fig. 2, the areas near the burst edges are brighter than those in the burst center because of their higher noise power. Azimuth scalloping can be modeled by a two-way azimuth antenna element pattern (AAEP), which is a function of the antenna steering angle as follows [21]:

$$G_{\mathrm{AAEP}}(\psi) = \mathrm{sinc}^2\left(\frac{L_{el}}{\lambda}\sin\psi\right) \tag{2}$$

where L_{el} is the antenna element length, λ is the radar's wavelength, and ψ is the antenna steering angle. Through the aft-fore antenna sweeping of the TOPSAR mode, the antenna steering angle is a linear function of the focused burst azimuth time [6], which is zero at the burst center. Fig. 3 shows the AAEP of the Sentinel-1 EW mode. Note that the focused burst length of the EW mode in a burst-merged image is approximately 3.04 s. Normally, this focused burst time-dependent antenna gain is to be compensated (descalloped) during the SAR processing step. However, this periodic variation is not reflected in the ESA-provided noise vectors. Recently, a filtering approach was proposed [22] and applied successfully for descalloping, but this is only a makeshift solution, which needs an adaptation of the filtering threshold for every application. In [21], it was noted that the descalloping gain is applied when the IPF removes noise from the images, but it is not applied when the IPF annotates the noise vectors. According to the Sentinel-1 Product Specification Manual [1], the thermal noise-level vector corresponding to any azimuth time is set to be obtained through the bilinear interpolation of the given noise vectors. This is not precise enough, because the scalloping gain changes periodically along the azimuth line. The effect of the scalloping gain on the noise power reaches up to 0.9 dB (see Fig. 3), which is significant for the cross-polarization channel, whose dynamic range is very limited for scatterers having small radar cross sections (RCSs). Note that the variation with the focused burst time is larger in the beam with a lower elevation angle, which means that the noise effect is larger as well.

III. Methods

To eliminate the residual noise in the ESA-provided noise-subtracted images, we suggest a three-step approach: 1) azimuth descalloping; 2) noise power scaling and interswath power balancing; and 3) local residual noise power compensation. Azimuth scalloping is related to the deterministic system parameters, and thus, this correction should be conducted first before proceeding with any further corrections. Noise power scaling and interswath power balancing are the modifications of the ESA-provided noise vectors and are the optimizations of the noise vectors for minimizing residual noise. Once the full noise field is retrieved, the corrections can be performed

by simple subtraction similar to the standard ESA method. As a final step, the residual noise power caused by the zero-clipping of negative-valued pixels is to be compensated locally. Note that the noise characteristics are all different in each subswath, because each subswath of TOPSAR was originally acquired using distinct system parameters and was processed individually before being merged. Thus, it is essential to separate the merged product back into a premerging state for proper noise elimination. Information on the subswath boundaries is available from the "Swath Merging Data Set Record" in the Level 1 Product Annotation file. Note that these records do not describe where the individual bursts were merged with regard to the azimuth within a swath.

A. Azimuth Descalloping

As shown in (2), the scalloping gain changes as a function of the antenna steering angle, and thus, it also changes as a function of the focused burst azimuth time. Since descalloping is not reflected in the ESA-provided noise vectors, a user needs to compute the scalloping gain for every azimuth line per subswath. The ESA provides auxiliary data used by the Sentinel-1 IPF to perform SAR processing through the Sentinel quality control webpage (https://qc.sentinel1.eo.esa.int), and the actual AAEP applied to Level 1 processing can be used for computing the azimuthal variations instead of using (2). The AAEP in the auxiliary data is given as a function of the steering angle, and the corresponding angle for each focused burst azimuth time should be calculated as follows [21]:

$$\psi(t) = \frac{\lambda}{2V_S} k_t t \tag{3}$$

$$k_t = -\frac{k_a k_s}{k_s - k_a} \tag{4}$$

where t is the focused burst azimuth time, V_S is the satellite velocity, k_a is the Doppler frequency rate induced by the relative velocity between the satellite and a scatterer, and k_s is the frequency modulation rate induced by the sweeping of the antenna.

Since the noise power shows the discontinuous changes at the interburst boundaries, it is important to find the burst center and boundary positions. However, precise timing information for each burst is not directly available from the Level 1 Product Annotation file. For the computation of the focused burst azimuth times, we used the times in the "Antenna Elevation Pattern Data Set Record," which are supposed to be updated by the IPF for every burst during image processing to match the zero-Doppler azimuth time of the first line of each burst in the full burst preserved single look complex (SLC) product. Since these time tags in the GRD product were simply copied from the SLC product, they must be corrected using the time differences between the "clipped" actual burst start positions and the "remaining" burst start positions in the GRD product. Fig. 4 shows how the scalloping gain changes with time and the appearance of the full burst and the merged burst. The scalloping gain is basically wrapped around the burst center position and repeats with each burst. The gray dotted line and the black solid line indicate the scalloping gains of the full burst and the merged burst, respectively. The annotated time

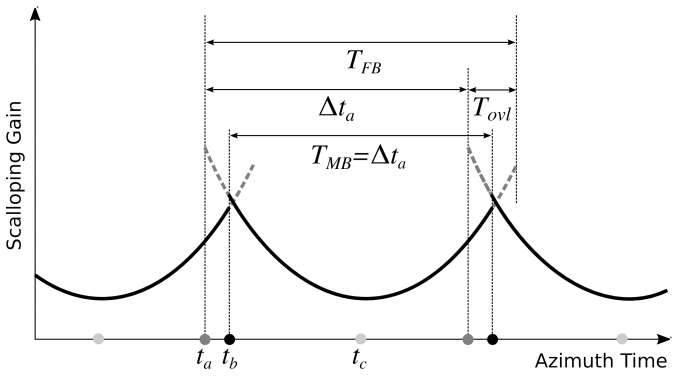

Fig. 4. Changes in the scalloping gain with the zero-Doppler azimuth time. The gray dotted lines represent the descalloping gain over the full burst duration (T_{FB}). t_a, t_b, and t_c indicate the time annotated in the antenna pattern record, the time at the burst margin in the burst-merged product, and the burst center time, respectively. The actual descalloping gain (solid line) repeats over every burst time duration T_{MB}.

t_a does not match with the actual interburst boundary t_b due to the clipped part. However, the burst center t_c can be found only if the full burst length T_{FB} is known, because the IPF cuts data of equal lengths from the early and late parts of each burst when the SLC slice is further processed into the GRD product

$$t_{c,n} = \frac{t_{a,n} + T_{\mathrm{FB}}}{2}. \tag{5}$$

Here, n is the burst number. The full burst length T_{FB} is computed as follows:

$$T_{\mathrm{FB}} = \frac{N_{az}}{N_{\mathrm{burst}} \cdot f_{az}} \tag{6}$$

where N_{az} is the number of azimuth lines in the subswath, N_{burst} is the number of bursts, and f_{az} is the sampling rate in the azimuth direction. Note that these parameters are from the SLC product; however, the corresponding values are available from the same Level 1 Product Annotation file of the GRD product. Since all the subswaths are already resampled to a common azimuth pixel spacing, f_{az} is the same for each subswath, but N_{az} is different for each subswath. Once T_{FB} is computed, the burst overlapping length T_{ovl} for each consecutive burst is

$$T_{\mathrm{ovl},n} = T_{\mathrm{FB}} - (t_{a,n+1} - t_{a,n}). \tag{7}$$

Then, this leads to the actual interburst boundary position as follows:

$$T_{b,n} = T_{a,n} + \frac{T_{\mathrm{ovl},n}}{2}. \tag{8}$$

To calculate the antenna steering angle (3), the zero-Doppler azimuth time must be wrapped around each burst center so that the resulting zero-Doppler azimuth times at all of the burst center are zero. In practice, the conversion from an "unwrapped" zero-Doppler time t to a "wrapped" focused burst time t_{burst} can be performed as follows:

$$t_{\mathrm{burst},n} = t - t_{c,n} \Rightarrow \left\{ t_{\mathrm{burst},n} \in \Re : -\frac{T_{\mathrm{ovr},n}}{2} \le t_{\mathrm{burst}} < \frac{T_{\mathrm{ovr},n}}{2} \right\}. \tag{9}$$

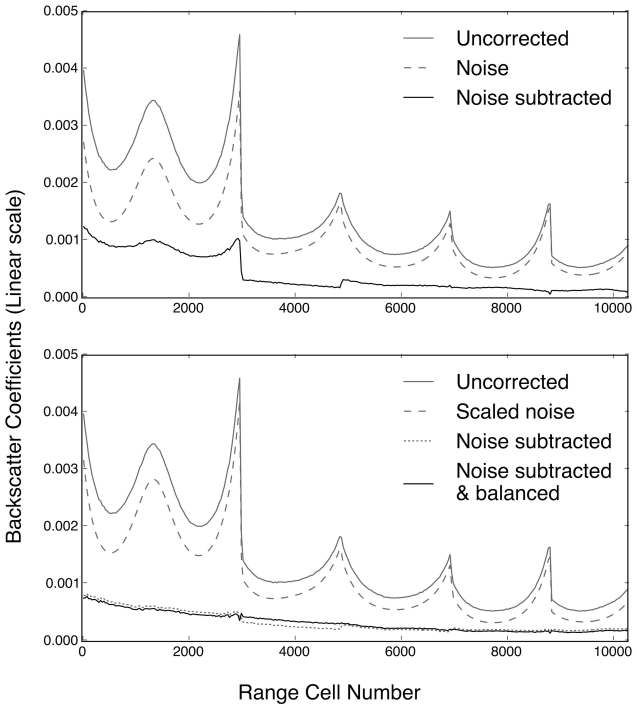

Fig. 5. Denoising results of noise subtraction using (Top) the raw ESA-provided noise vectors and (Bottom) the scaled noise. The HV channel raw backscatter coefficients are from a calm sea surface, which is expected to vary smoothly for all observation angles of Sentinel-1. The noise subtraction result using the scaled noise shows a smoother variation compared with the results from using the raw ESA-provided noise vectors. Note that interswath power balancing is required afterward in order to link the subswath boundaries (Scene ID: S1A_EW_GRDM_1SDH_20160124T171219_20160124T171323_009639_00E0BC_4327).

Once the focused burst time is calculated, the corresponding antenna steering angle is calculated using (3) and (4), and then, a lookup table of the AAEP [G_{AAEP}, see Fig. 3 (top)] is used to compute the descalloping gain for each subswath

$$G_{\mathrm{ds,ssw}} = \frac{1}{G_{\mathrm{AAEP,ssw}}(\psi(t_{\mathrm{burst}}))}. \tag{10}$$

This descalloping gain G_{ds} should be applied to a given noise field, which is obtained by the linear interpolation between the ESA-provided noise vectors.

B. Noise Power Scaling

If the noise power in the ESA-provided noise vectors does not match with the real noise in an image, then the noise will be undercompensated or overcompensated, such that the resultant profile contains residual distortions, which are correlated with the noise floor itself. When the background consists of homogeneous and low-backscattering materials, most of the energy recorded in the cross-polarized channel comes from thermal noise, and any noise-correlated pattern should disappear after noise correction. Fig. 5 shows the mean range profile of an HV channel of an EW GRD product over a calm sea surface. According to previous studies [23], [24], a cross-polarization channel has little dependence on the incidence angle, and thus, variations in the noise-corrected profile should be almost flat over the entire range of cells. However, as shown in Fig. 5 (top), which shows the results of denoising using the ESA-provided noise vectors, the mean range profile after noise removal seems to need an extra correction. For subswath EW1 (the leftmost 3000 cells), it is easy to recognize that the thermal noise was undercompensated, because the denoised signal and the noise are positively correlated. By assuming that a "correct" noise removal should result in a smoothly sloped profile, one can find a suitable scaling factor to apply to the ESA-provided noise vectors. The optimum scaling factor can be found by minimizing the residual sum of squares (RSS) of the weighted linear fit of the denoised signal, which is calculated as follows:

$$s(k) = \sigma^0_{\mathrm{SN}} - k \cdot G_{\mathrm{ds}} \cdot \sigma^0_N \tag{11}$$

$$\mathrm{RSS}(k) = \sum_{i=1}^{N} w_i (\hat{s}_i(k) - s_i(k))^2 \tag{12}$$

where σ^0_{SN} is the raw sigma nought before noise subtraction, σ^0_N is the NESZ computed from the ESA-provided thermal noise vector, $s(k)$ is the denoised sigma nought, which is the difference between σ^0_{SN} and the scaled σ^0_N by a scaling factor k, w is the weight factor, i is the range cell number, N is the total number of range cells in the given subswath, and $\hat{s}(k)$ is the linear fit model for the denoised signal $s(k)$. The noise vectors in all the subswaths have common characteristics insomuch that the noise-level variations at the subswath boundary are larger than at the subswath center. Since the purpose of the linear fit is to find the optimal scaling factor that results in the most effectively flattened range profile over a homogeneous surface, weighting factors were introduced to ensure that the more undulating parts have higher weights than the other parts. If the denoised signal is corrupted mostly by thermal noise, the undulating parts will reside mostly in the region where the undulation of the pure thermal noise is high. In this paper, we used the absolute value of the gradient of the ESA-provided noise vectors as a proxy to finding this undulating part, which is thus used as a weighting factor in (12). The denoised profile often has negative power at this stage; however, since the proposed scheme is only based on measuring the linearity (flatness) of the denoised profile, the negative power does not cause any problems. When the RSS is a minimum among the RSSs of the regression models with varying scaling factors, that specific regression model most effectively fits the denoised signal, because the denoised profile is smoothed best by the adequate subtraction of noise. In this way, the optimal noise scaling factor K_{ns} can be determined for each subswath

$$\min_{k \in \Re} \{\mathrm{RSS}(k)\} \Rightarrow K_{\mathrm{ns,ssw}} = k. \tag{13}$$

Here, $\mathrm{ssw} = \{1, \ldots, 5\}$ is the subswath number.

In Fig. 5 (bottom), an example of scaled noise and the noise subtraction results is presented. We applied the noise scaling factors of 1.09, 0.92, 0.97, 0.89, and 0.82 for each subswath (EW1–EW5). The resulting denoised profile is smoother than the one in the top, and it does not seem to be correlated with the noise profile.

C. Interswaths Power Balancing

By adopting noise scaling, the most affected parts are found near the subswath margins, as the noise powers in these parts are higher than those in the subswath center. After applying noise scaling, the signal power differences between the subswath margins must be estimated and compensated to prevent discontinuities. Computing these offsets for power balancing can be accomplished by connecting the margins of neighboring subswaths. To avoid being affected too much by local fluctuations, the best linear fit model used for evaluating the noise scaling factor can be reused to compute the initial balancing power at the swath margin as follows:

$$\begin{aligned} K^0_{\text{pb},1} &= 0 \\ K^0_{\text{pb,ssw}} &= (\alpha_{\text{ssw}-1} i + \beta_{\text{ssw}-1}) - (\alpha_{\text{ssw}} i + \beta_{\text{ssw}}) \end{aligned} \tag{14}$$

where α_{ssw} and β_{ssw} are the slope and intercept of linear fit model for the subswath index number ssw $= \{2, \ldots, 5\}$, and i is the range pixel number of the interswath boundary. Since there are only four interswath boundaries, the balancing power for the first subswath is set as zero for now. In this stage, a modified noise power $\sigma^0_{N,\,\text{mod}}$ can be computed by combining K_{ns}, K^0_{pb}, and G_{ds} as follows:

$$\sigma^0_{N,\,\text{mod}} = K_{\text{ns}} \cdot G_{\text{ds}} \cdot \sigma^0_N + K^0_{\text{pb}}. \tag{15}$$

To maintain radiometric consistency, the total power in $\sigma^0_{N,\,\text{mod}}$ must be adjusted to that of σ^0_N. For this bias correction, the mean difference between the two noise powers is added to the computed interswath balancing power

$$K_{\text{pb}} = K^0_{\text{pb}} + \left\langle \sigma^0_N - \sigma^0_{N,\,\text{mod}} \right\rangle. \tag{16}$$

Here, $\langle \cdot \rangle$ indicates an averaging operator. Now, the balancing power for EW1 is not zero, and the total noise power in the ESA-provided noise vectors can be conserved in the modified noise field. Fig. 5 (bottom) shows the results from before and after interswath power balancing.

D. Noise Subtraction

By combining the three abovementioned modification factors, a complete 2-D noise field can be reconstructed and then subtracted from the raw sigma nought as follows:

$$\begin{aligned} \sigma^0_{S,\text{ssw}} &= \sigma^0_{\text{SN,ssw}} - \left(K_{\text{ns,ssw}} \cdot G_{\text{ds,ssw}} \cdot \sigma^0_{N,\text{ssw}} + K_{\text{pb,ssw}}\right) \\ \text{ssw} &= \{1, \ldots, 5\}. \end{aligned} \tag{17}$$

The reconstructed noise (the terms in the parentheses) has the same form as (15), but the bias-corrected balancing power K_{pb} is used in this instance. Since each subswath has a different corresponding correction factor, the individual processes should be performed separately and then combined back into one using the "Swath Timing Data Set Record" in the Level 1 Product Annotation file.

E. Local Residual Noise Power Compensation

Since the noise subtraction process can result in negative power values, which cannot be handled in subsequent processing steps, such as decibel conversion, the pixels with negative values should be replaced by nonnegative values or not a number in many cases. The most common method is to clip the negative values to zero; however, this usually leads to the undercompensation of the noise power. To remove the radiometric bias and to retain the total power locally, we adopted the local SNR-dependent radiometric correction developed in [20]. Since the occurrence of negative power will increase as the local SNR decreases, the bias originating from zero-clipping will increase as well. This bias can be avoided by subtracting the locally more greatly scaled noise power so that the results of zero-clipping and local extra scaling cancel out in a statistical sense

$$\sigma^0_S = \begin{cases} \sigma^0_{\text{SN}} - \gamma \cdot \sigma^0_S, & \sigma^0_{\text{SN}} > \sigma^0_S \\ 0 & \text{otherwise.} \end{cases} \tag{18}$$

Here, γ is an extra noise scaling factor, which is equal to one when there is no zero-clipped pixel locally, and it becomes greater than one when zero-clipping occurs. For an efficient implementation of this local correction, γ should be defined as a function of the SNR in advance. A lookup table can be constructed by using a sliding patch analysis as suggested in [20]. Measurements of the SNR and γ in local patches (e.g., a subwindow of 3×3, 5×5, or 7×7 pixels) over many noise-subtracted images are required, but a large computational effort can be avoided during practical implementation by using a lookup table rather by measuring the local extra scaling factor every time.

IV. Results

A. A. Noise Correction Coefficients

To find the optimal scaling factors and offsets for the ESA-provided noise vectors, we measured them from many Sentinel-1A dual-polarization (HH/HV) images over the open ocean. We collected and analyzed 535 images acquired from March 19, 2015 to May 31, 2016 over the Norwegian Sea. For each image, we divided the entire image into five azimuthal blocks and acquired the averaged range profile for each block to minimize speckle noise. This process allows for five independent measurements per image, and thus, the total number of range profile data was 2665. Since the proposed noise-scaling scheme is based on measuring the flatness of the denoised profile, the input data do not necessarily need to have very low backscatter as long as the RCS in the scene varies smoothly and monotonically. However, the use of profile parts with backscatters that are slightly too high in addition to slowly varying intensities may lead to overestimated noise scaling factors; thus, we discarded the use of profiles having powers higher than the estimated noise power by 3 dB. For each image, the RSSs of the linear fits of the scaled and noise-subtracted range profiles were evaluated with a scaling factor varying from 0 to 2 with a step of 0.01. By taking an average of all the measurements, optimized noise scaling factors were determined for each of the subswaths. Then, the scaling factors were applied to the ESA-provided noise vectors again to measure the interswath balancing power for each image. The coefficient optimization for the interswath

TABLE I
NOISE SCALING AND INTERSWATH POWER BALANCING COEFFICIENTS

IPF version	Parameters	Coefficients for each subswath				
		EW1	EW2	EW3	EW4	EW5
2.4x [*a] *(Mar.2015-)*	K_{ns} [*b]	1.209 ± 0.048	0.953 ± 0.044	1.031 ± 0.047	0.982 ± 0.035	0.913 ± 0.078
	K_{pb} [*c]	-1.940 ± 0.056	-1.553 ± 0.980	-0.723 ± 0.620	-0.439 ± 0.651	-0.343 ± 0.813
2.5x *(Jul. 2015-)*	K_{ns}	1.197 ± 0.045	0.942 ± 0.045	1.017 ± 0.045	0.974 ± 0.037	0.909 ± 0.073
	K_{pb}	-2.716 ± 0.066	-2.839 ± 0.836	-1.119 ± 0.563	-0.365 ± 0.574	-0.338 ± 0.748
2.6x *(Nov. 2015-)*	K_{ns}	1.133 ± 0.046	0.933 ± 0.058	0.960 ± 0.062	0.912 ± 0.049	0.843 ± 0.096
	K_{pb}	-2.780 ± 0.108	-2.477 ± 1.079	-0.677 ± 0.736	1.094 ± 0.610	1.173 ± 0.830
2.7x *(Apr. 2016-)*	K_{ns}	1.363 ± 0.062	0.991 ± 0.053	1.043 ± 0.077	0.990 ± 0.036	0.932 ± 0.097
	K_{pb}	-2.602 ± 0.184	-3.553 ± 1.018	-2.661 ± 0.712	-2.289 ± 0.578	-2.106 ± 0.860

[*a] For data processed with IPF version 2.4x, which is not calibrated for noise, pre-scaling is applied.
[*b] K_{ns} = Noise scaling coefficients
[*c] K_{pb} = Inter-swath power balancing coefficients. The values need to be scaled by 10^{-4}.

power balancing process was conducted in the same way by taking the average of all the measurements.

In Table I, we summarized the mean and standard deviation values of the scaling and power-balancing coefficients for each subswath. We divided the resulting coefficients into four groups according to major changes in the IPF versions. Since the different IPF versions might have different Level 1 processing details (e.g., gain setting and adopting/discarding filtering processes), the IPF version must be considered when interpreting the resulting coefficients. The differences in the Level 1 processing methods essentially yield different noises [5]. Addressing the details as to how a particular processing parameter change in each IPF version contributes to the noise field is a complex subject and is beyond the scope of this paper. Changes in the first digit after the decimal point of the IPF version indicate major modifications, and changes in the second digit reflect minor alterations. Note that the noise vectors included in IPF 2.4× are not calibrated and have significantly smaller values compared with those in the calibrated noise vectors. For exploiting a long-term evaluation, it is highly valuable to extend the applicability of our method even earlier to a prenoise calibration phase (before July 2015). By adopting adequate prescaling to the given noise vectors, it is possible to conduct the same investigation of the noise correction coefficients. These prescaling values can be found in the same auxiliary calibration data file containing the AAEP under the tag name of "noiseCalibrationFactor" (see [25]). After applying prescaling, the range of the resulting coefficients was similar to those of the calibrated versions.

As noted in Section III-B, a scaling coefficient that is greater than one indicates that the ESA-provided noise vectors were underestimated, and thus, a stronger noise power correction is required. The noise scaling coefficients for the different IPF versions have some common features, such as distinctly high numbers in subswath EW1 and numbers that are similar to one another in the other subswaths (EW2-5). The standard deviations were not small when considering the deviation between the obtained mean values and one (i.e., no scaling) for

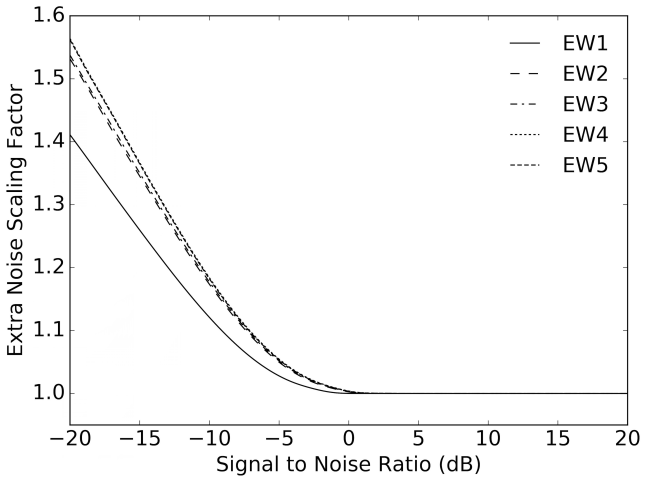

Fig. 6. Estimated extra noise scaling factors for each subswath. The values increase as the SNR decreases.

subswaths EW2-5; however, the large differences between the scaling coefficient of EW1 and those of the other subswaths are very clear. The interswath balancing powers for the different IPF versions also show some common features. The overall negative numbers reflect that the radiometric bias in the initial measurements of the interswath power balancing coefficient K_{pb}^{0} is negative in all cases, because the noise scaling for EW1 is much greater than one, which leads to a higher noise power than the ESA-provided noise vectors. The balancing powers increase as the subswath number increases. This means that the use of the corrected noise results in the subtraction of stronger noise in near-range subswaths and the subtraction of weaker noise in far-range subswaths. This does not imply that the proposed correction introduces a radiometric bias, because the direct use of the ESA-provided noise vectors clearly causes more distorted/unbalanced noise subtraction results, which will be shown in Section IV-B.

The extra noise scaling coefficients are shown in Fig. 6. We used the same data set for noise scaling and interswath

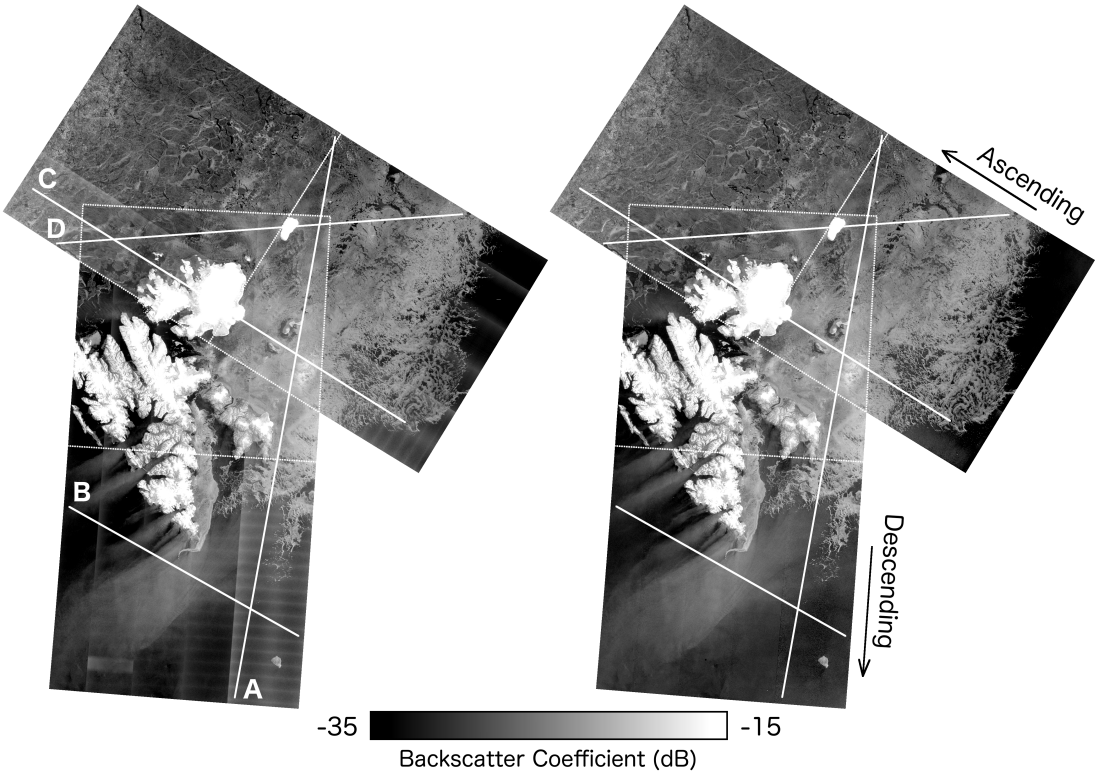

Fig. 7. One-day (April 27, 2016) mosaic image over Svalbard. Strong scalloping and interswath discontinuities are retained in the correction results using (Left) raw ESA-provided noise vectors, while (Right) proposed method results in a noise-free image.

power balancing coefficient measurements to construct this lookup table. For each image, and after the subtraction of noise using the coefficients in Table I, the local SNR and extra noise scaling factors were estimated by using a sliding analysis patch of 5×5 pixels. The use of a patch smaller than this often failed in computing the SNR due to the existence of consecutively negative-powered pixels, while the use of a larger patch yielded a bad adaptation to the local characteristics of the signal. In Fig. 6, as the SNR decreases, the extra noise scaling factors increase correspondingly. Since the GRD product is already multilooked, and it is thus speckle reduced, the numbers are small in comparison with the case of the SLC product in [20].

During the computation of the optimal coefficients, we only used HH-/HV-polarization data; however, the same method can be applied to VV/VH polarization data as well. Since the proposed method is based on the tuning of given noise vectors, a similar strategy could even be applied to other SAR systems, such as RADARSAT-2 ScanSAR.

B. Performance Evaluation

To evaluate the benefit of the proposed method, we compared the denoising results of the proposed method with those from the unscaled, original ESA-provided noise vectors for three different cases. It must be noted that we used the correction coefficients in Table I for the denoising in the following experiments.

First, we made a mosaic image for examining the enhancement in the visual interpretability. Fig. 7 shows a one-day mosaic image over Svalbard (two paths and four frames). The notable residual noise in the image processed using the unscaled ESA noise vectors [see Fig. 7 (left)] is largely reduced in the image processed using the proposed method [see Fig. 7 (right)]. The backscatter coefficients of the four profiles A–D are drawn in Fig. 8 for a closer quantitative comparison. Scalloping was successfully corrected (the first 300 km part in A), and the interswath discontinuities (two sharp changes at the positions of 50 and 280 km in B) were removed by applying the proposed method. There were fewer visibly distinct changes, but the backscatter coefficients from the ascending and descending paths over the overlapped parts matched better in the results of the proposed method (i.e., the gaps between the solid lines are smaller than those between the dashed lines in C and D). Note that the absolute values of the backscatter coefficients from the ascending and descending paths are different because of the differences in the incidence angle and observation time. An enhanced visual interpretability is still one of the most important aspects for a sea ice analyst to construct an SAR image-based sea ice chart. In a similar manner, the proposed denoising method can contribute to many kinds of applications using a mosaic of Sentinel-1 images.

Second, the correction performance for a nonwater surface was investigated. Because of the nature of additive noise, the correction will be most effective when the signal intensity is close to the NESZ. For higher surface backscatter, a lower relative noise power corruption is observed. Fig. 9 shows two different sigma nought profiles over the open

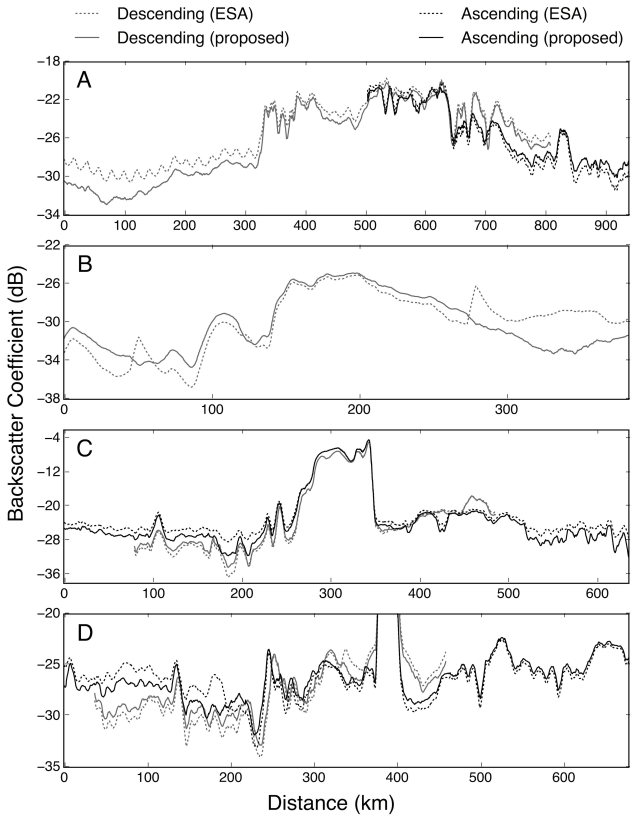

Fig. 8. Profiles of the sections in Fig. 7. Dotted lines: correction results using the raw ESA-provided noise vectors. Solid lines: proposed method.

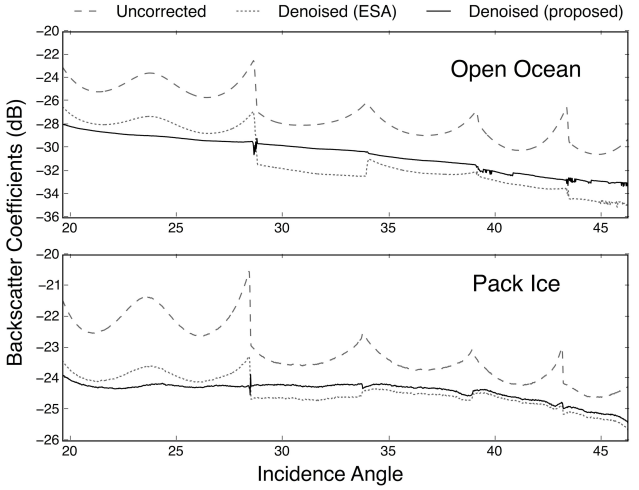

Fig. 9. Averaged sigma nought values of (Top) open water from 112 images centered in the northern part of the North Atlantic Ocean and (Bottom) dense pack ice from 104 images near the geographic North Pole. The time window is one year (August 2015–July 2016).

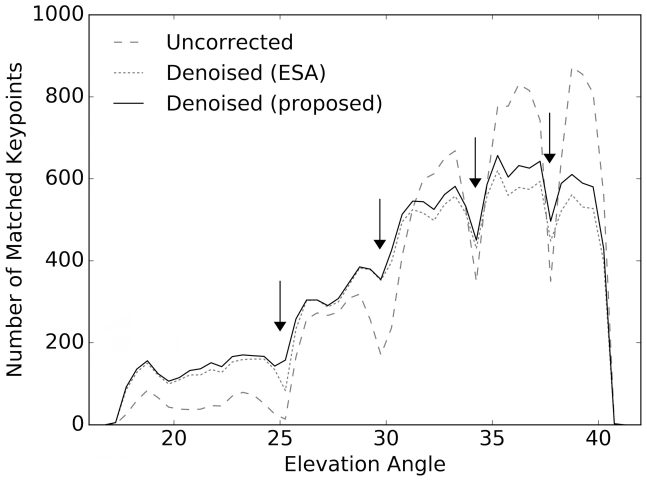

Fig. 10. Number of keypoints found by applying a sea ice drift retrieval algorithm [26]. Arrows: swath boundary positions.

ocean and dense pack ice. For each surface type, the sigma nought profiles obtained from 112 and 104 scenes over one year (August 2015–July 2016), respectively, were investigated. In both cases, the uncorrected raw profile (dashed line) contains the influence of strong noise. The denoising result using the proposed method (solid line) shows a better performance in terms of noise suppression and discontinuity reduction than that using the subtraction of the unscaled original ESA-provided noise vectors (dotted line). For the open ocean, the performance is comparable with that in Fig. 4, which is corrected using optimized parameters for each specific image. In each subswath, the resulting signal seems well flattened, which indicates that noise scaling factors retrieved from many independent images work fairly well in any open ocean image. However, there are small discontinuities of approximately 0.2 dB in between EW3 and EW4 (around an incidence angle of 39°). For the pack ice, both the flattening of the subswaths and the interswath balancing show the effectiveness of the proposed method, but with slightly less effectiveness. Again, there are also notable discontinuities in between EW3 and EW4. Although the proposed method produced better results compared with those using the ESA-provided noise vectors, the residual shape indicates that the proposed correction method and/or the estimated noise level in the noise packets in the GRD product are imperfect. Since the residual noise from the direct use of the ESA-provided noise vectors shows an inconsistent pattern for the two different surface types (i.e., undercompensation for the open ocean but slightly overcompensation for the pack ice, except for subswath EW1), there might be some uncertainty in the estimated noise level of the noise packets in the downlinked raw data itself. The noise pulses are recorded only at the start and end of each data acquisition [26], which normally reaches up to a few tens of minutes. This means that the actual noise level could not match the annotated noise level if the true noise level changes between two different measurements.

Third, an enhancement in the measurement of sea ice drift was investigated. We used a feature-tracking algorithm [27], which detects keypoints from two images for the purpose of matching them. The keypoint search is performed based on finding an object that has a sufficient intensity contrast; thus, noise correction directly affects the algorithm performance. We used 215 pairs taken over sea ice between Svalbard and the North Pole in January 2016. Fig. 10 shows a comparison of the number of keypoints found from an uncorrected image and two types of denoised results. The proposed method (solid line) yielded a superior performance in all the elevation angles

compared with the ESA method (dotted line). Compared with the results from using the uncorrected image, denoising generated a large increase in the number of features found at low elevation angles (17°–30°) and along interswath boundaries (indicated by arrows in Fig. 10); there were, however, some decreases at high elevation angles over 32°. The relative performances of the denoised images compared with the uncorrected image based on the number of total keypoints found were 97.5% and 103.9% for the ESA method and the proposed method, respectively. Komarov and Barber [19] found that noise floor stripes in RADARSAT-2 images do not affect the motion tracking performance of the pattern-matching algorithm. Similarly, Muckenhuber *et al.* [27] reported that the noise removal did not improve the motion tracking performance of the feature-tracking algorithm. This is true for denoising using the ESA-provided noise vectors in terms of the number of total keypoints found. The large asymmetry in the distribution of keypoints in Fig. 7 is partly due to the higher noise at low angles and the ice-water contrast variability with the incidence angle. The increased number of keypoints at low angles indicates that the proposed method reduced the contribution of noise effectively. For motion tracking, an even spatial distribution of keypoints is as important as the total number of keypoints, which means that the proposed denoising method can certainly improve the performance of the feature-tracking algorithm.

V. Conclusion

We developed an efficient noise reduction method for Sentinel-1 GRD products by tuning the ESA-provided noise vectors with empirically determined correction coefficients. Through extensive experimentation, we measured the optimal coefficients for noise scaling and interswath power balancing. The resulting coefficients showed different noise characteristics for different IPF versions.

The proposed method corrects not only the range-dependent thermal noise power but also the burst time-dependent scalloping noise. By combining the scaled and power-balanced noise vectors with the scalloping gains, it is possible to reconstruct a complete noise field for noise subtraction. In this paper, the following results were obtained.

1) Although the scalloping effect is not reflected in the ESA-provided noise vectors, it should be applied to the reconstructed noise field, because it can cause radiometric errors of the NESZ up to 0.9 dB, which is significant considering the relatively low sigma nought in the cross-polarization channel.
2) EW1 is largely undercorrected and has a much higher power than the other subswaths when the original ESA-provided noise vectors are used for noise subtraction. We suggest the optimum coefficients for noise scaling and interswath power balancing. The coefficients depend on the IPF version.
3) The proposed noise correction results in clear improvements for applications that are based on image intensity analyses, including noise-free multitemporal image mosaicking, smooth continuous radiometric measurements over the whole incidence angle range in the EW mode, and an increased performance of feature-tracking algorithms.

Although we only showed three examples to demonstrate the benefits of applying the proposed denoising method, there are other potential improvements to many kinds of intensity analysis-based applications. Based on the results presented in this paper, we conclude that the proposed method is beneficial for promoting and broadening the use of Sentinel-1 TOPSAR GRD data.

References

[1] *Sentinel-1 Product Specification*, document S1-RS-MDA-52-7441, Issue 3/3, 2016. [Online]. Available: https://sentinel.esa.int/documents/247904/349449/Sentinel-1_Product_Specification

[2] *RADARSAT-2 Product Format Definition*, document RN-RP-51-2713, Issue 1/15, 2016. [Online]. Available: https://mdacorporation.com/docs/default-source/technical-documents/geospatial-services/radarsat-2-product-format-definition

[3] *TerraSAR-X Ground Segment Basic Product Specification*, document TX-GS-DD-3302, Issue 1.9, 2013. [Online]. Available: http://sss.terrasar-x.dlr.de/docs/TX-GS-DD-3302.pdf

[4] F. D. Carsey, *Microwave Remote Sensing of Sea Ice* (Geophysical Monograph Series). Washington, DC, usa: AGU, 1992.

[5] U. Balss, H. Breit, and A. Niedermeier, "Computation of signal gain and noise gain of a SAR processor," presented at the CEOS SAR Workshop, Noordwijk, The Netherlands, Oct. 2015. [Online]. Available: http://sarcv.ceos.org/site_media/media/documents/balss_et_al_slides.pdf

[6] F. D. Zan and A. M. M. Guarnieri, "TOPSAR: Terrain observation by progressive scans," *IEEE Trans. Geosci. Remote Sens.*, vol. 44, no. 9, pp. 2352–2360, Sep. 2006.

[7] A. Meta, J. Mittermayer, P. Prats, R. Scheiber, and U. Steinbrecher, "TOPS imaging with TerraSAR-X: Mode design and performance analysis," *IEEE Trans. Geosci. Remote Sens.*, vol. 48, no. 2, pp. 759–769, Feb. 2010.

[8] N. Gebert, G. Krieger, and A. Moreira, "Multichannel azimuth processing in ScanSAR and TOPS mode operation," *IEEE Trans. Geosci. Remote Sens.*, vol. 48, no. 7, pp. 2994–3008, Jul. 2010.

[9] S. Leigh, Z. Wang, and D. A. Clausi, "Automated ice–water classification using dual polarization SAR satellite imagery," *IEEE Trans. Geosci. Remote Sens.*, vol. 52, no. 9, pp. 5529–5539, Sep. 2014.

[10] N. Zakhvatkina, A. Korosov, S. Muckenhuber, S. Sandven, and M. Babiker, "Operational algorithm for ice–water classification on dual-polarized RADARSAT-2 images," *Cryosphere*, vol. 11, pp. 33–46, Jan. 2017, doi: 10.5194/tc-11-33-2017.

[11] C. Brekke and S. N. Anfinsen, "Ship detection in ice-infested waters based on dual-polarization SAR imagery," *IEEE Geosci. Remote Sens. Lett.*, vol. 8, no. 3, pp. 391–395, May 2011.

[12] A. Marino, W. Dierking, and C. Wesche, "A depolarization ratio anomaly detector to identify icebergs in sea ice using dual-polarization SAR images," *IEEE Trans. Geosci. Remote Sens.*, vol. 54, no. 9, pp. 5602–5615, Sep. 2016.

[13] P. W. Vachon and J. Wolfe, "C-band cross-polarization wind speed retrieval," *IEEE Geosci. Remote Sens. Lett.*, vol. 8, no. 3, pp. 456–459, May 2011.

[14] P. A. Hwang, W. Perrie, and B. Zhang, "Cross-polarization radar backscattering from the ocean surface and its dependence on wind velocity," *IEEE Geosci. Remote Sens. Lett.*, vol. 11, no. 12, pp. 2188–2192, Dec. 2014.

[15] R. Lucas *et al.*, "An evaluation of the ALOS PALSAR L-band backscatter—Above ground biomass relationship Queensland, Australia: Impacts of surface moisture condition and vegetation structure," *IEEE J. Sel. Topics Appl. Earth Observ. Remote Sens.*, vol. 3, no. 4, pp. 576–593, Dec. 2010.

[16] N. Miranda *et al.*, "S-1A product performance status," presented at the CEOS SAR Workshop, Noordwijk, The Netherlands, Oct. 2015. [Online]. Available: http://sarcv.ceos.org/site_media/media/documents/CEOS_S1_IPF_PRODUCTS.pdf

[17] W. Albright and J. Nicoll, "Empirical determination of thermal noise levels in synthetic aperture radar," in *Proc. IGARSS*, Toronto, ON, Canada, Jun. 2002, pp. 2729–2731.

[18] A. Korosov, N. Zakhvatkina, and S. Muckenhuber, "Ice/water classification of Sentinel-1 images," in *Proc. EGU Gen. Assembly*, Vienna, Austria, Apr. 2015, paper EGU2015-12487-1.

[19] A. S. Komarov and D. G. Barber, "Sea ice motion tracking from sequential dual-polarization RADARSAT-2 images," *IEEE Trans. Geosci. Remote Sens.*, vol. 52, no. 1, pp. 121–136, Jan. 2014.
[20] U. Balss, H. Breit, and T. Fritz, "Noise-related radiometric correction in the TerraSAR-X multimode SAR processor," *IEEE Trans. Geosci. Remote Sens.*, vol. 48, no. 2, pp. 741–750, Feb. 2010.
[21] *Sentinel-1 Level-1 Detailed Algorithm Definition*, document SEN-TN-52-7445, Issue 2/0, 2016. [Online]. Available: https://sentinel.esa.int/documents/247904/1877131/Sentinel-1-Level-1-Detailed-Algorithm-Definition
[22] J. Karvonen, "Baltic sea ice concentration estimation using SENTINEL-1 SAR and AMSR2 microwave radiometer data," *IEEE Trans. Geosci. Remote Sens.*, vol. 55, no. 5, pp. 2871–2883, May 2017.
[23] B. Zhang, W. Perrie, and Y. He, "Wind speed retrieval from RADARSAT-2 quad-polarization images using a new polarization ratio model," *J. Geophys. Res.*, vol. 116, no. C8, p. C08008, Aug. 2011, doi: 10.1029/2010JC006522.
[24] J. W. Sapp, S. O. Alsweiss, Z. Jelenak, P. S. Chang, S. J. Frasier, and J. Carswell, "Airborne co-polarization and cross-polarization observations of the ocean-surface NRCS at C-band," *IEEE Trans. Geosci. Remote Sens.*, vol. 54, no. 10, pp. 5975–5992, Oct. 2016.
[25] *Masking, No-value, Pixels on GRD Products Generated by the Sentinel-1 ESA IPF*, document MPC-0243, Issue 1.0, 2015. [Online]. Available: https://sentinels.copernicus.eu/documents/247904/2142675/Sentinel-1-masking-no-value-pixels-grd-products-note
[26] *Sentinel-1 Level-0 Product Format Specifications*, document S1PD.SP.00110.ASTR, Issue 1/7, 2012. [Online]. Available: https://earth.esa.int/documents/247904/349449/Sentinel-1_Level-0_Product_Format_Specification.pdf
[27] S. Muckenhuber, A. A. Korosov, and S. Sandven, "Open-source feature-tracking algorithm for sea ice drift retrieval from Sentinel-1 SAR imagery," *Cryosphere*, vol. 10, pp. 913–925, Apr. 2016, doi: 10.5194/tc-10-913-2016.

Jeong-Won Park (S'08–M'13) received the B.S. and Ph.D. degrees in Earth system sciences from Yonsei University, Seoul, South Korea, in 2006 and 2013, respectively.

From 2014 to 2015, he was a Post-Doctoral Researcher with the Division of Polar Ocean Environment, Korea Polar Research Institute, Incheon, South Korea. He is currently a Post-Doctoral Researcher with the Ocean and Sea Ice Remote Sensing Group, Nansen Environmental and Remote Sensing Center, Bergen, Norway. His research interests include sea ice classification, ice shelf dynamics, synthetic aperture radar (SAR) signal processing, and the development of SAR Doppler applications.

Anton A. Korosov received the Ph.D. degree in oceanography from Russian State Hydrometeorological University, St. Petersburg, Russia, in 2007.

From 2002 to 2010, he was a Researcher with the Nansen International Environmental and Remote Sensing Center, St. Petersburg. Since 2011, he has been a Researcher with the Ocean and Sea Ice Remote Sensing Group, Nansen Environmental and Remote Sensing Center, Bergen, Norway. His research interests include algorithms for retrieval of sea ice parameters from satellite Earth observation data, ocean optical remote sensing, and the development of satellite data management systems.

Mohamed Babiker received the M.S. and Ph.D. degrees in hydrology from Bergen University, Bergen, Norway, in 1999 and 2004, respectively.

He has more than 15 years of experience using the remote sensing and geographic information system for satellite data processing in the polar regions covering sea ice mapping, iceberg detection, and glaciers monitoring. He has been involved in several scientific cruises in the arctic. He has been the deputy coordinator of several EU projects. He is currently a Research Scientist with the Nansen Environmental and Remote Sensing Center, Bergen. He is also the Project Manager of the SONARC Project. He has been active in the European Space Agency funded polar projects and related national and international activities at the Nansen Center for over ten years.

Stein Sandven received the Cand.real degree in physical oceanography with the University of Bergen, Bergen, Norway, in 1979.

He has more than 30 years of experience in polar research with main expertise in marine and cryosphere remote sensing, polar oceanography, and sea ice research. He has been a coordinator of many research projects funded by EU, European Space Agency, Norwegian Space Center, Norwegian Research Council, and industry over the last 25 years. He is currently the Research Director with the Nansen Environmental and Remote Sensing Center, Bergen, and an Adjunct Professor with The University Centre in Svalbard, Longyearbyen, Svalbard and Jan Mayen. He is also the Science Leader of the ESA CCI Project on sea ice and a Coordinator of the EU Project INTAROS with about 50 partners from 20 countries.

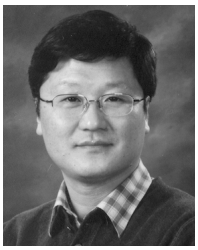

Joong-Sun Won (S'92–M'93–SM'03) received the B.S. and M.S. degrees in geology and geophysics from Yonsei University, Seoul, South Korea, in 1983 and 1985, respectively, and the Ph.D. degree in geophysics from the University of Manitoba, Winnipeg, MB, Canada, in 1993.

From 1993 to 1996, he was a Senior Scientist with the Marine Geology Division, Korea Ocean Research and Development Institute, Ansan, South Korea. Since 1996, he has been a Professor with Yonsei University, where he is currently a Professor with the Department of Earth System Sciences. His research interests include remote sensing, tidal flats, geohazard, signal processing, radar interferometry, and velocity retrieval from synthetic aperture radar data.